Available online at www.sciencedirect.com
ScienceDirect
Fluid Dynamics Research 40 (2008) 95–122
FLUID DYNAMICS RESEARCH

Internal wave focusing revisited; a reanalysis and new theoretical links

Frans-Peter A. Lam*, Leo R.M. Maas

Royal Netherlands Institute for Sea Research (NIOZ), P.O. Box 59, 1790 AB Texel, The Netherlands

Received 28 March 2006; received in revised form 19 January 2007; accepted 7 February 2007
Available online 8 March 2007
Communicated by Edgar Knobloch

Abstract

An experiment which discussed the appearance of an internal wave attractor in a uniformly stratified, free-surface fluid [Maas, L.R.M., Benielli, D., Sommeria, J., Lam, F.-P.A., 1997. Observation of an internal wave attractor in a confined, stably stratified fluid. Nature 388(6642), 557–561] is revisited. This is done in order to give a more detailed and more accurate description of the underlying focusing process. Evolution of the attractor can now be quantified. For the tank with one sloping sidewall, and for the parameter regime (density stratification, forcing frequency) studied, the inverse exponential growth rate determined at several locations in the fluid turns out to be 122 s always. Only the start and duration of the growth differed: away from the attractor region it appeared later and of shorter duration. Here, these features are interpreted by employing a new theoretical basis that incorporates an external forcing via a surface boundary condition (an infinitesimal barotropic seiche) and that describes the solution in terms of propagating waves.

Keywords: Wave attractor; Internal gravity waves; Laboratory experiment; Stratified fluids; Focusing; Fluid dynamics

1. Introduction: internal waves in a confined fluid domain

Internal waves in a continuously stratified fluid, represented by the stability frequency $N(z)$, have peculiar characteristics. We will discuss the case with constant N, which supports internal waves of

* Corresponding author. Present affiliation: TNO, Underwater Technology Department, P.O. Box 96864, 2509 JG The Hague, The Netherlands. Fax: +31 70 374 0654.
E-mail address: Frans-Peter.Lam@tno.nl (F.-P.A. Lam).

0169-5983/$32.00
doi:10.1016/j.fluiddyn.2007.02.003

frequency $\omega < N$ (Groen, 1948). For monochromatic internal waves, energy propagates obliquely through the fluid with a fixed angle to the vertical θ, set by the ratio $\omega/N = \cos\theta$, see e.g. Turner (1973). The behavior of propagating internal waves in such a stratified fluid is well suited for a description in terms of rays. As depicted for example in Turner (1973, Fig. 2.10), reflection of waves at solid boundaries of orientation other than horizontal or vertical gives rise to divergence or convergence of wave energy. Maas and Lam (1995), from here on referred to as ML, demonstrate that in almost all confined fluid domains focusing dominates over defocusing. The result is that wave energy focuses onto a limit cycle, called *wave attractor*. Maas, Benielli, Sommeria, and Lam (1997) (in the following referred to as MBSL) subsequently observed the existence of such an internal wave attractor around the predicted location. The experiment qualitatively showed that the wave attractor developed on a time scale lasting several tens of wave periods. Interestingly, the wave field appeared to grow initially as a standing wave and evolved subsequently into a propagating wave as the final stationary state.

However, the aforementioned experimental study neither quantified the wave's detailed evolution in terms of growth rate and transition from standing to propagating, nor the spatial structure of its amplitude and phase fields. It also lacked a quantitative description in terms of the applied forcing. This was due to the peculiar nature of the theoretical internal wave field whose stream function field was given as a standing, free wave that appeared to be uniquely prescribed once the pressure was set in two specific boundary intervals only (ML). This seems to contrast on the one hand with the propagating character of the observed asymptotic state of the wave field, and on the other hand with the intuitive notion that one should be free to apply pressure at the boundary in whatsoever interval one pleases. The aim of this paper is to bridge this gap between the theoretical description and the experimentally observed nature of the internal wave attractor. This is done by adding forcing to the theory and by providing a quantification of the experimental wave field. For this reason, the phenomenon of geometric focusing, underlying the appearance of a wave attractor, will be recapitulated in the next section. In Section 3 the laboratory experiment will be revisited and the evolution of the wave field will be quantified. The previously mentioned restriction on the prescription of the pressure at the boundary will be removed in Section 4, when propagating solutions to the forced problem are discussed. The paper ends with a summary and discussion. A review of wave attractors, which discusses also those that arise in confined, homogeneous rotating fluids due to focusing of inertial waves, can be found in Maas (2005).

2. Earlier theoretical results

2.1. Geometric focusing

ML theoretically studied multiple reflections of internal wave rays (characteristics) in a confined two-dimensional fluid. Different geometrical basin shapes were explored: rectangular, parabolic, elliptic and trapezoidal. It was concluded that in almost all two-dimensional geometries internal waves are focused onto a limiting set of characteristics: the wave attractor. Rieutord and Noui (1999) showed that this included also the geophysically relevant spherical shell. Exceptional boundary shapes are formed by rectangles and ellipses. These are nonfocusing as long as these are not tilted with respect to the direction of gravity, because otherwise they would feature wave attractors too (Ogilvie, 2005; Kopecz, 2006). The attractor (limit-cycle) can be classified by the number of surface reflections, called the *period* of the attractor, which is related to the rotation number (Manders et al., 2003; Kopecz, 2006). The period

of the attractor remains the same over a finite interval of the lumped parameter

$$\tau = \left(\frac{N^2}{\omega^2} - 1\right)^{1/2} \frac{D}{L}$$

defined by stratification (buoyancy frequency), N, internal wave frequency, ω, and the basin's aspect ratio, D/L, where L and D are the half-width and depth of the basin, respectively (ML). Some basin shapes, apart from those mentioned above, possess a residual symmetry. In such basins, for specific values of τ a so-called global resonance can occur. In this case, ray convergence is exactly balanced by divergence of the reflecting wave rays and each ray is periodic by closing upon itself. In rectangular basins such a global resonance is known as an internal seiche, in which no convergence or divergence of reflected wave energy occurs at all.[1] However, in continuously stratified fluids, confined to basins of arbitrary shape, this global resonance should be considered as the exception rather than the rule, both in the laboratory as well as in nature. Generically, the attractor dominates the internal wave appearance. This leads to a solution with much fine scale structure which denies the alleged dominance of large-scale modes in confined fluid systems (Baines, 1997; Thorpe, 2003).

In fact, as ML argued, not only do large-scale eigenmodes in general no longer dominate the response of confined, continuously stratified fluids, but, remarkably, they even no longer exist. It is this property that inhibits the classical approach in which one derives an equation for the evolution of the wave field's amplitude of a particular eigenmode.

An example of an internal wave attractor of rectangular shape is given in Fig. 1a. The topography is the same as in MBSL: a trapezoid with one sloping side wall. The lumped parameter τ defines the bottom's

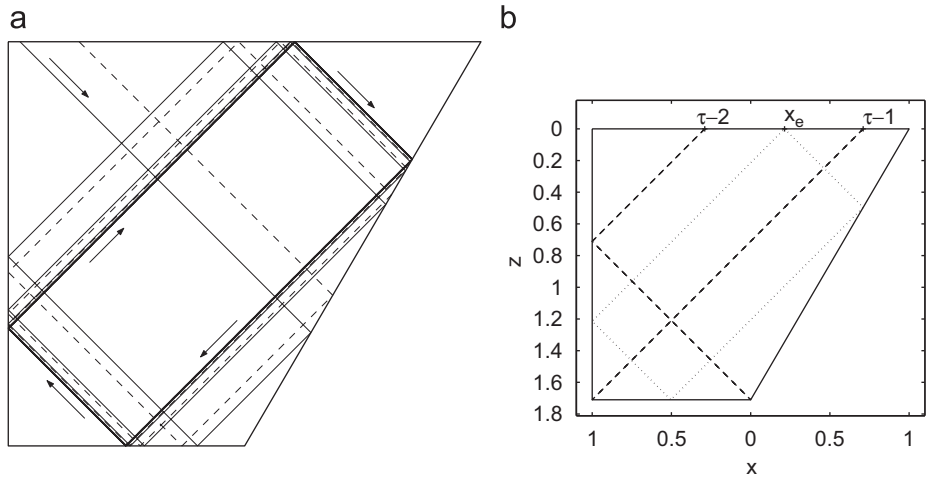

Fig. 1. (a) Example of internal wave ray focusing (thin solid and dashed lines) and wave attractor (thick solid line) in a trapezoidal geometry with the bottom at $z = -\tau$; $\tau = 1.71$. (b) Positions of special points at the surface define primary fundamental intervals, see the discussion in the text. The attractor, having surface reflection at $x_e = \tau^2 - \tau - 1$, is depicted with dotted lines.

[1] We here address only waves in a continuously stratified fluid; internal seiches, describing interfacial waves, are not considered. For two-layer systems with a stratified deep layer and a homogeneous top layer, the strength of the pycnocline, separating these two layers, determines the scattering (trapping, reflection and transmission) of waves (Gerkema, 2001).

'virtual' depth over the flat part: $z = -\tau$, for $-1 \leqslant x \leqslant 0$, and upward slope, $z = -\tau(1 - x)$, for $0 < x \leqslant 1$. The attractor is reached by the characteristic webs that are constructed by launching two characteristics from the upper left part of the surface towards the right (solid and dashed lines, respectively). In a monochromatic wave, energy propagates downwards along such rays, see arrow in upper left part. In the two-dimensional case, the rays along which the energy propagates are identical with the mathematical characteristics of the governing differential equation; in three dimensions this holds only approximately (Harlander and Maas, 2006). Following the adage that the waves maintain their angle with respect to the direction of gravity, two half-webs are formed by these characteristic segments together with their subsequent boundary reflections. The other half-webs are obtained by launching leftward. Each web combines these half-webs and approaches the attractor. The energy 'encircles' the attractor in one definite, clockwise sense (see other arrows).

For this simple geometry, the dependence of the attractor on the lumped parameter, τ, and on a second parameter, that determines the horizontal position of the foot of the slope, is fractal (MBSL) and contains Arnol'd tongues (Manders et al., 2003). For the configuration shown in Fig. 1a, and for $1 < \tau < 2$, the attractor has a period 1 orbit with only one surface reflection located at $x_e = \tau^2 - \tau - 1$. For the example of Fig. 1 ($\tau = 1.71$) this is at $x_e = 0.2141$.

2.2. Standing wave solution

In order to relate the experimentally observed velocity field to the 'ray-web' that was found geometrically in Fig. 1a, we first recall how to obtain the stream function from the web. This procedure was referred to as the 'dressing of the web', see MBSL and Maas (2005).

The basin can be seen as a peculiar kind of billiards. As mentioned above, the ray-structure of the internal waves imposed by geometry, internal wave frequency and stratification is such that upon reflection from a boundary the ray keeps its angle fixed with respect to the vertical (gravity). By stretching the vertical coordinate, this fixed angle can be made 45° for any monochromatic frequency. The stretching is then present in the scaled depth τ. Owing to incompressibility, the velocity field, (u, w), is described in terms of the stream function $\Psi(x, z, t)$: $u = -\partial\Psi/\partial z$ and $w = \partial\Psi/\partial x$. We study monochromatic waves: $\Psi(x, z, t) = \mathrm{Re}[\psi(x, z)\exp(-\mathrm{i}\omega t)]$, where Re[..] signifies the real part. The spatial part of the stream function is governed by the hyperbolic equation (ML): $\partial^2\psi/\partial x^2 - \partial^2\psi/\partial z^2 = 0$. This implies that the stream function can generally be expressed as

$$\psi = f(x - z) - g(x + z) \tag{1}$$

and similarly the (properly scaled) reduced pressure

$$p = f(x - z) + g(x + z). \tag{2}$$

These solutions are given in terms of the partial pressures $f(s)$ and $g(s)$, where s is a characteristic coordinate. The partial pressure is constant on the sloping characteristics. In order to make the solutions unique, the partial pressure is prescribed along two specific parts of the surface of the basin only (ML). For the unforced internal wave problem, the free surface is assumed to be quiescent and the fluid domain's boundary is a streamline: $\psi = 0$. This boundary consists of segments at surface ($z = 0$), wall ($x = -1$), and bottom ($z = -\tau h(x)$), where $h(x)$ represents the bottom shape, with $|h| \leqslant 1$. Applying this condition along the surface implies $g(s) = f(s)$. But, in order for the stream function to vanish also at any other point of the boundary, the value of f set at the incident characteristic needs to be conserved upon reflection and thus

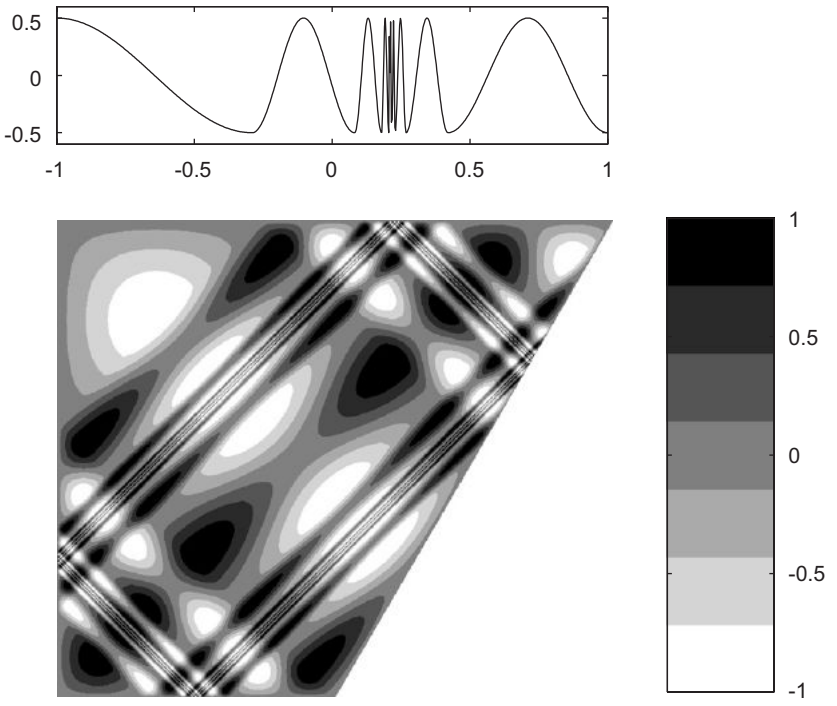

Fig. 2. Example of standing wave solution $\psi(x, z)$ for a surface pressure $p_a(x) = 2f(x)$ that is prescribed within the two fundamental intervals defined in Fig. 1b. From these, the whole pressure distribution along the surface, as indicated in the top panel, can be inferred. Values for ψ are coded with the gray scale as shown in the legend on the right.

sets the value at the reflected characteristic. For real-valued functions $f(s)$, this presents a standing wave solution and in this case the surface pressure is $p_a(x) = 2f(x)$. However, because the partial pressure is (instantaneously) preserved along characteristics, the same value of f is passed to neighboring surface intervals when following internal wave rays. This means that we are not free to specify the pressure along the whole boundary, but only within the so-called fundamental intervals. The largest of these are the two aforementioned intervals which are therefore called *primary* fundamental intervals (see Fig. 1b). Prescribing the pressure in fundamental intervals defines the pressure over the whole surface. An example similar to that of ML and MBSL is given in Fig. 2.[2] At the surface, the primary fundamental intervals for this basin (and for $1 < \tau < 2$) are $x \in [-1, \tau - 2]$ and $x \in [\tau - 1, 1]$. The boundaries of these surface intervals are obtained by connecting the corners of the basin with the surface along characteristics (see Fig. 1b). Prescribing $f(x)$ over these intervals, the remainder of $f(x)$ can be inferred, see the top panel of Fig. 2.

Since ψ is real, the *standing* wave solution of Fig. 2 is oscillating synchronously; it is *blinking*. Lacking forcing, it is a *free wave*. Thus, to obtain a unique solution the pressure is prescribed at the surface within the aforementioned fundamental intervals, but the prescription itself is still arbitrary. Physically it is unsatisfactory that one is required to prescribe the pressure strictly on just two intervals, indeed without

[2] The example depicted in Fig. 2 is shown on an (arbitrary) xz-grid. However, it should be stressed that this solution is *not* a numerical approximation. For each element (x_i, z_j) on the grid, the corresponding (analytical) solution ψ_{ij} is *exact*.

a link to the actual forcing. In Section 4 we will lift this restriction by considering a possibly realistic forcing mechanism that allows the prescription of a specific pressure field also beyond these two intervals. It leads to a propagating wave solution, similar to that observed. But first, in the next section, we will have a closer look at the experimental results.

3. The internal wave attractor experiment revisited

3.1. Original analysis

MBSL observed the existence of an internal wave attractor in a laboratory experiment. The experiment was carried out in a uniformly stratified tank, with a sloping sidewall and free surface, as in Fig. 1. The platform on which the tank was placed was oscillating vertically with angular frequency 2ω, in this way slightly modulating the restoring force of gravity. The response in the fluid takes place by parametric excitation. Each fluid particle, seen as an individual oscillator, is then subject to a buoyancy oscillation, similar to a pendulum whose point of suspension is forced to oscillate vertically. The forcing is most effective when the suspension is forced to go down when the pendulum is in either of its extreme upward (leftward or rightward) positions, hence when the forcing has a frequency twice that of the pendulum. In a similar fashion, modulation of gravity at frequency 2ω excites subharmonic waves of frequency ω in the stratified fluid. Mathematically, the modulation of gravity appears as an extra sinusoidal temporal restoring term of the harmonic oscillator, of period $T = 2\pi/\omega$. This extended oscillator equation is known as the Mathieu equation (Bender and Orszag, 1978). Benielli and Sommeria (1998) studied parametric excitation both in a two-layer fluid as well as in a uniformly stratified fluid in a rectangular basin. It was the latter configuration that was used in MBSL by inserting a sloping wall. We will therefore compare results with those obtained in the rectangular tank.

Several frequencies close to that used in Fig. 1 have been explored in MBSL, and confirmed the existence of the period-1, or (1, 1) internal wave attractor in the interval $1 \leqslant \tau \leqslant 2$. Here, we refer to an (m, n)-attractor as one having m reflections from the surface and n from the vertical side wall. In the experiment, at the edges of the (1, 1)-attractor frequency interval, somewhat higher forcing amplitudes (15 cm) were needed to excite the attractor than the threshold amplitude of 8 cm for central frequencies. The attractor was visualized by monitoring the position of eight layers of fluorescent dye that were stimulated by laser light.

The most prominent result of MBSL was that in the experiment the predicted presence, shape and location of a (1, 1) internal wave attractor are reproduced, see Fig. 3. Approximately 5 min ($\sim$ 70 wave periods) after the oscillation of the tank was started, localized fluid motion became visible. The attractor first showed up as a smooth, *standing-wave pattern* (Fig. 3; top), in which the region around the attractor oscillated synchronously. Later, the elevations of the dye layers showed a distinct propagating behavior around the attractor. This can be seen from the inward propagation of white 'nodal' (phase) lines, indicated by arrows in the bottom panels of Fig. 3. Inward (outward) propagation of similar nodal lines can be observed along the other long (short) branches of the attracting rectangle. Since the dispersion relation of internal waves predicts energy to propagate perpendicularly to the phase propagation direction (such that phase and group speed have opposite vertical components), it was inferred that energy propagates clockwise around the attractor, consistent with the direction into which the slope focuses reflecting characteristics (Fig. 1a).

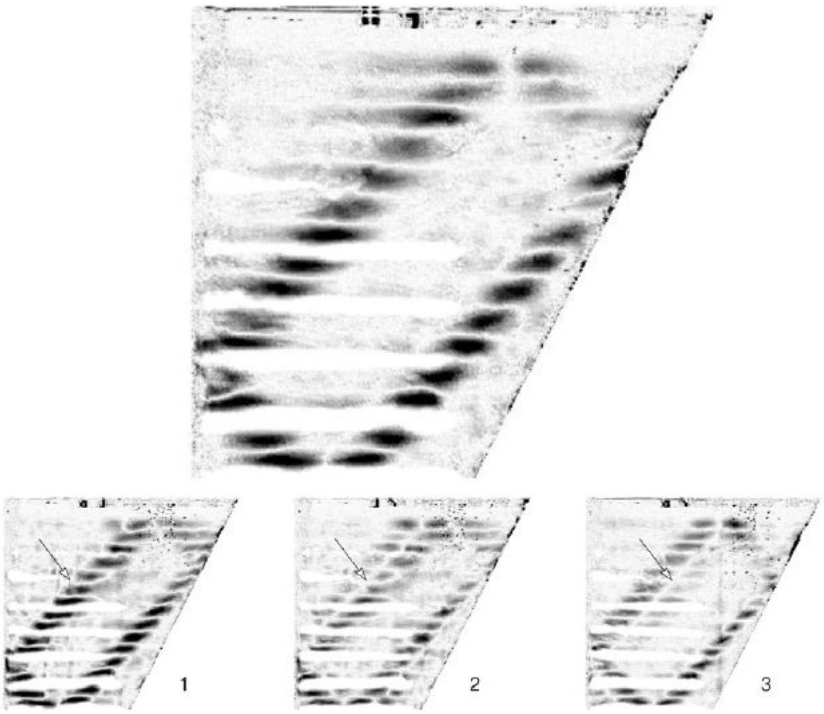

Fig. 3. Wave attractor observed in laboratory experiment (black-and-white version of Fig. 4 of MBSL). The attractor is visualized by highlighting the absolute difference (compared to some reference image) of the intensity of the video image. In this way, large displacements of originally horizontally oriented dye bands are visible. Here $\tau = 1.71$ and forcing amplitude is 10 cm. Pictures show growth phase (top), taken 9 min after start of experiment and permanent stage (bottom), after 10 min, showing images at three instances in a wave cycle at $t/T = n/12$, labeled by integer $n = 1, 2, 3$.

The two observed phases were called the growth and permanent phase respectively (MBSL). The standing behavior in the growth phase was explained qualitatively in terms of waves that are generated locally in the bulk of the fluid and that travel with equal magnitude in opposite directions on each characteristic. Waves excited on different parts of a characteristic that propagate towards each other thus set up a standing wave. Later, in the permanent phase, however, half of these waves pass the repellor (ML) and change the sense in which they traverse the basin. Thus, regardless of initial propagation direction, these waves then all wind around the wave attractor in the same, clockwise sense, giving the attractor's near-field its ultimate propagating character.

In the next subsection digitized images from the video recording of the experiment will be analyzed in a more quantitative way. Especially, the growth rate of the amplitudes and the standing versus propagating nature of elevations will be examined.

3.2. Revisiting the wave-attractor experiment

In one of the experiments in MBSL, discussed below (see Table 1and Fig. 3), the forcing amplitude of the table oscillation was set to 10 cm and the forcing frequency $2\omega = 2.88\,\mathrm{s}^{-1}$. This led to an internal wave period $T_\mathrm{w} = 2\pi/\omega = 4.37\,\mathrm{s}$.

Table 1
Parameters and scales used in MBSL (Maas et al., 1997)

Length	$2L$	261	mm
Depth	D	261	mm
Width	W	96	mm
Amplitude	Z	80–150	mm
Stratification	N	1.89	s^{-1}
Experiment 4			
Amplitude	Z	100	mm
Time scale	T	4.36	s
Period	T_w	4.37	s
Frequency	$\omega = \frac{2\pi}{T_w}$	1.438	s^{-1}
Scaled depth	$\tau = \frac{D}{L}\sqrt{\frac{N^2}{\omega^2} - 1}$	1.71	–

The video recording of this experiment was digitized, and translated to 25 images for each second, with a resolution of 256×224 pixels each. The experiment lasted over 20 min, taking more than 31,000 images in total. We analyze the evolution of the intensity of all pixels for all images during the experiment. Details of the image and time series analysis can be found in the Appendix. We will express vertical excursions in terms of the scalar pixel intensity that changes from 80 (no dye) to 240 (within the dye layers). While it is not easy to assign a vertical displacement to any particular change in pixel intensity, we can get some indication from the following observation. Each of the eight pairs of dyed and undyed layers is about 3.2 cm thick. So, a change from minimum to maximum intensity occurs over vertical displacements of about 1.6 cm or more. There are indications that such displacements can reach up to 3.5 cm. This can be inferred from the passage of neighboring dye layers. This also implies that it is difficult to assign an unbiased phase to any change in pixel intensity. An increase of pixel intensity can either mean the downward displacement of the upper or upward displacement of the lower neighboring dye layer. In the following this ambiguity has usually been eliminated by computing phase modulo 180°, which, however, does not allow us to distinguish upward from downward motion. In one case, for a single time frame, also this final ambiguity was eliminated and the phase was computed modulo 360°.

Subsequently, each time series of pixel intensity is harmonically analyzed. In particular the amplitude and phase of the wave of frequency ω is determined at each pixel. Fig. 4 displays the amplitude and phase field (in this case modulo 360°) at $t/T = 160$, which is the moment that the attractor is most sharply defined. The harmonic amplitude field has a similar localization of wave energy as that revealed by the snapshots in the bottom panel of Fig. 3. The harmonic phase aligns itself along the four branches of the attractor, with inward (outward) phase propagation along the long (short) branches labeled 1 and 3 (2 and 4) in Fig. 5b. This confirms the earlier observed propagation of nodal lines. Also note in particular the out-of-phase character of the two pairs of opposite attractor branches, which, again, is consistent with clockwise energy propagation.

3.3. Composite harmonic amplitude and phase across the attractor

In order to see the slow-time evolution of the amplitude and phase fields, the previous analysis is repeated every wave period (see Appendix). A composite picture, showing the development of the wave

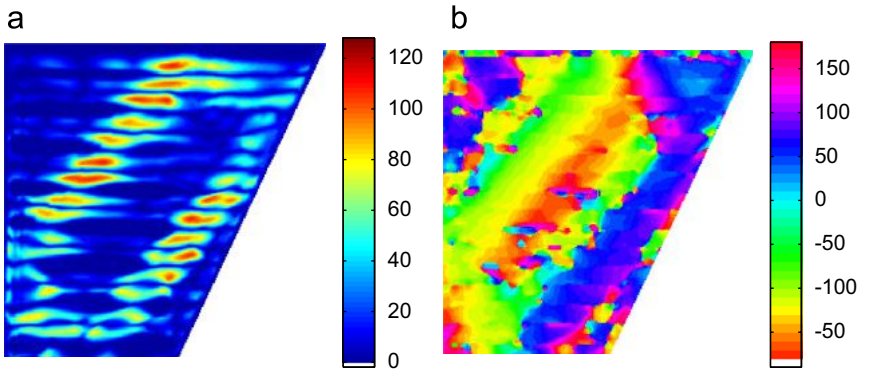

Fig. 4. Example of harmonic amplitude (a) and phase (b, in degrees, see legend) of pixel intensity taken from same period as images in bottom panel of Fig. 3: $t/T = 160$. Here phase is corrected by checking for sudden jumps in vertical direction. The relation between pixel intensity and vertical displacement is discussed in the text.

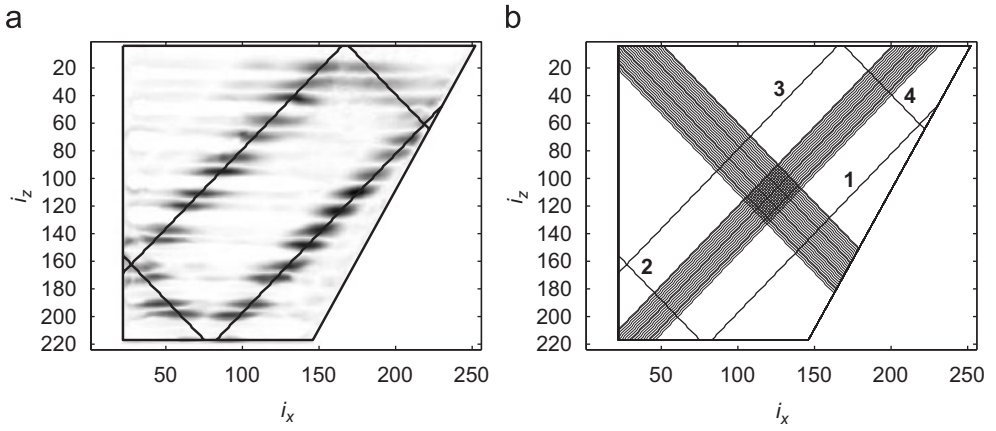

Fig. 5. Overview of location of the attractor, based on a sample image (a, left) and selected lines used for composite 'waterfall' plot (b, right). The numbering of the four attractor branches refers to the order in which energy propagates along the attractor, upon the focusing reflection from the slope. In subsequent figures (6–9), horizontal pixel index i_x of the longest lines (starting at $i_x = 23$ in the upper and lower left corner of the tank) will be used as along-ensemble co-ordinate (from left to right).

attractor, is obtained by filling the artificial gaps (see e.g. Fig. 5a) that are caused by the finite width of the dye bands used to visualize vertical displacements. This filling is done by 'averaging' over an ensemble of characteristics that cross the attractor transversely, see Fig. 5b. The ensembles consist of 27 (downward to the right) or 19 (upward to the right) diagonal, neighboring characteristics. For the amplitude field, averaging consists in taking the maximum of the ensemble; for the phase, taking its median value (modulo 180°), as in Fig. A3b. This is possible because the oscillation is in phase along each individual branch of the internal wave attractor (Fig. 4). These average values are assigned to the horizontal pixel index coordinate, i_x, corresponding to the ensemble's central characteristic.

The amplitudes observed along the long branches 1 and 3 of the attractor (Fig. 6) are higher than those along the short branches 2 and 4 (Fig. 7). The weakest amplitudes are found at branch 4 (Fig. 5b). It

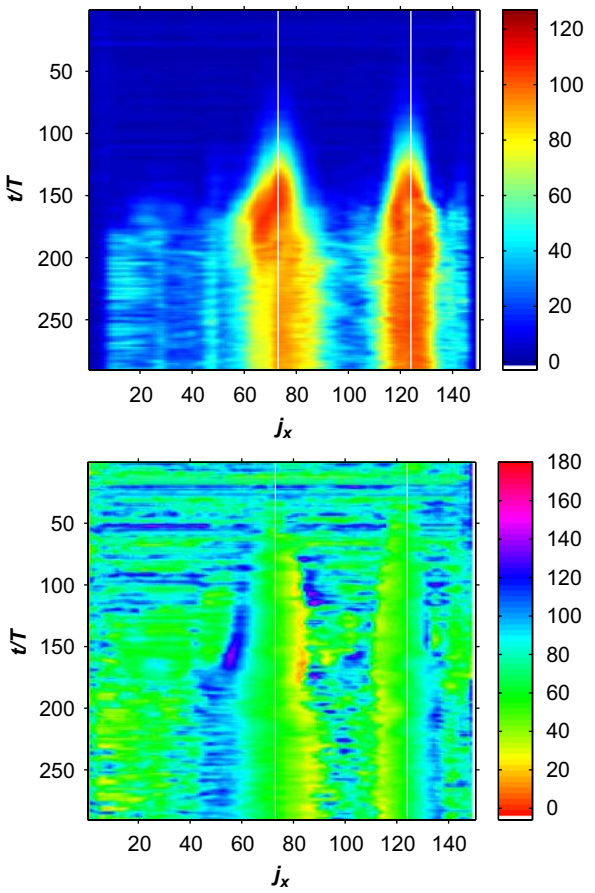

Fig. 6. Composite waterfall plot of maximum of harmonic amplitude (top) and median of harmonic phase (bottom) along 27 characteristics crossing the long branches, 1 and 3, of the attractor, as depicted in Fig. 5. Phase, modulo 180°, is similarly defined as in the Appendix. For waterfall plots, time is represented on the vertical axis (increasing from the top downwards) and the horizontal pixel index on the horizontal axis. The theoretically predicted attractor crossings are depicted with vertical white lines at index $j_x \equiv i_x - 22 = 73$ and 124, corresponding to $i_x = 95$ and 146, respectively.

is not clear why this happens. The characteristics are symmetric with respect to the vertical, and hence the projection of the true, oblique motion on the vertical direction is the same for both characteristic directions. Also, since both the bottom, left side wall and surface are all nonfocusing it is not clear where this change in amplitude comes from. Clearly, the different stages can be recognized again; the first discernable motion around the attractor location appears around $t/T = 60$. Until $t/T = 100$ the phase is uniform near the attractor, and this corresponds with the standing wave phase. From $t/T = 100$ to 170 the attractor grows and starts to develop a propagating character, until finally ($t/T > 170$) the high amplitude motion smears out and the quasi-stationary permanent phase appears.

The clear transition from the initial standing to final propagating wave behavior, Fig. 3, is in this analysis seen to take place gradually. Figs. 6 and 7 (bottom panels) show that in the initial stages of the experiment the phase (modulo 180°) is quite uniform around the attractor (characterized by the single green color).

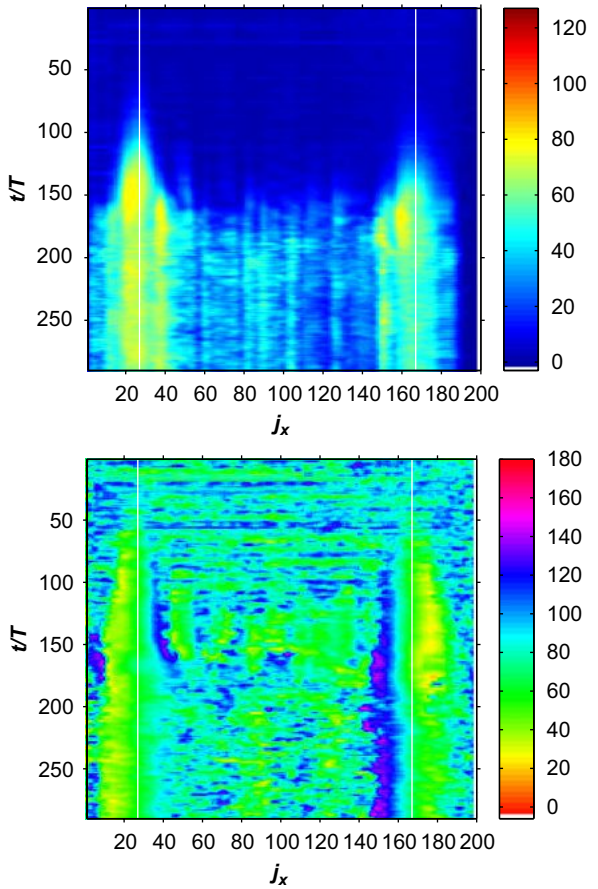

Fig. 7. As Fig. 6 but for 19 characteristics crossing the short branches 2 and 4 of the attractor (see Fig. 5). The original estimated attractor crossings are depicted with vertical white lines at $j_x = 27$ and 167 ($i_x = 49$ and 189).

Subsequently, the high-amplitude bands around the attractor beams amplify and broaden until their width stays constant for $t/T > 170$. During the same transition period the phase develops a persistent phase gradient across the two branches of the attractor. Defining $j_x \equiv i_x - 22$, in Fig. 8 this can be seen in pixel range $55 < j_x < 83$ and $115 < j_x < 135$. These gradients are consistent with the propagating phase observed in terms of the motion of a nodal line in MBSL. This is indicative of the previously inferred clockwise energy propagation around the attractor. Surprisingly, the net observed phase variation (nearly 60°, see Fig. 8) amounts to just part of the expected cross-beam variation of 180°, valid for a stationary internal wave beam affected by linear dispersion and viscous damping (Lighthill, 1978). This difference is presumably limited by the range over which the amplitude stands out over the noisy background.

3.4. Second harmonic

Fig. 9 gives amplitude (top) and phase (bottom) of the second harmonic in terms of its ensemble maximum and median values, respectively. It is clear that the amplitude starts to grow around the attractor

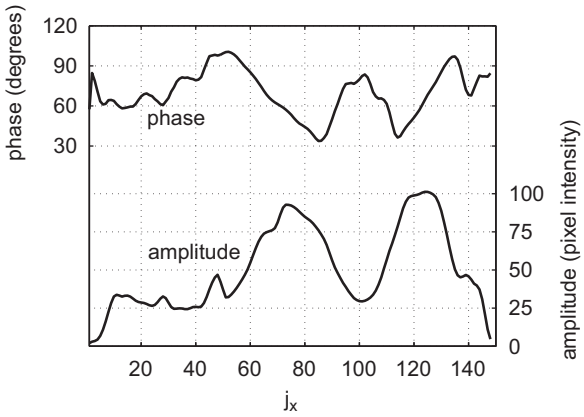

Fig. 8. Mean phase and amplitude distributions along the beam perpendicular to the long branches, 1 and 3, of the attractor for the last 50 sequences ($t/T = 240$–290) of Fig. 6.

a little later (around $t/T = 135$; 9.8 min) then for the fundamental harmonic ω. After having reached a maximum value around $t/T = 155$ (11.3 min), the amplitudes decrease again. Amplitudes for 2ω are always lower than for ω; phases show a larger gradient in the across-attractor direction.

This second harmonic can occur through a number of causes which we list here. Internal waves with frequency 2ω might first be directly forced, as a secondary instability of the Mathieu equation (Bender and Orszag, 1978). Second, they may be generated due to nonlinear advection of overlapping internal wave beams (Peacock and Tabaei, 2005; Gostiaux et al., 2006). However, in this experiment they are not expected to propagate away as free waves because they are above the buoyancy frequency ($2\omega > N$). Hence, when these second harmonics do show up, this could imply that they are forced locally. Their trapping, along the attractor that corresponds to frequency ω, suggests this to be a continuous process, occurring all along the attractor. Third, as discussed in the Appendix, double-frequency motion might also be an artifact. This is merely a problem of the tracer used in the experiment. The double-frequency amplitude would show up when the single frequency motion is saturated and the vertical component of fluid elevations equals or exceeds the width of the dye bands. However, the expected associated decrease in the single-frequency amplitude is not clearly visible. Finally, the presence of second (and other) harmonics may reflect the nonlinear nature of the cross-beam structure that propagates in the cross-beam direction during each wave period.

3.5. Exponential growth

In Fig. 10, the inverse exponential growth rate, τ_g, is estimated for some vertical cross-sections of Figs. 6 and 7. This is obtained by modeling the evolution of the pixel intensity during a definite time interval as $e^{(t-t_0)/\tau_g}$, for some starting time t_0. For all (seven) cross-sections examined, this inverse growth rate is estimated as $\tau_g = 122 \pm 5$ s. Outside the attractor the pixel intensity starts to grow later (larger t_0), which indicates remote forcing, and the intensity saturates at a lower level (owing to a shorter growth duration), but it increases at exactly the same rate as within the attractor neighborhood. These properties are quite unlike the growth of a classical eigenmode, for which growth duration, the moment at which

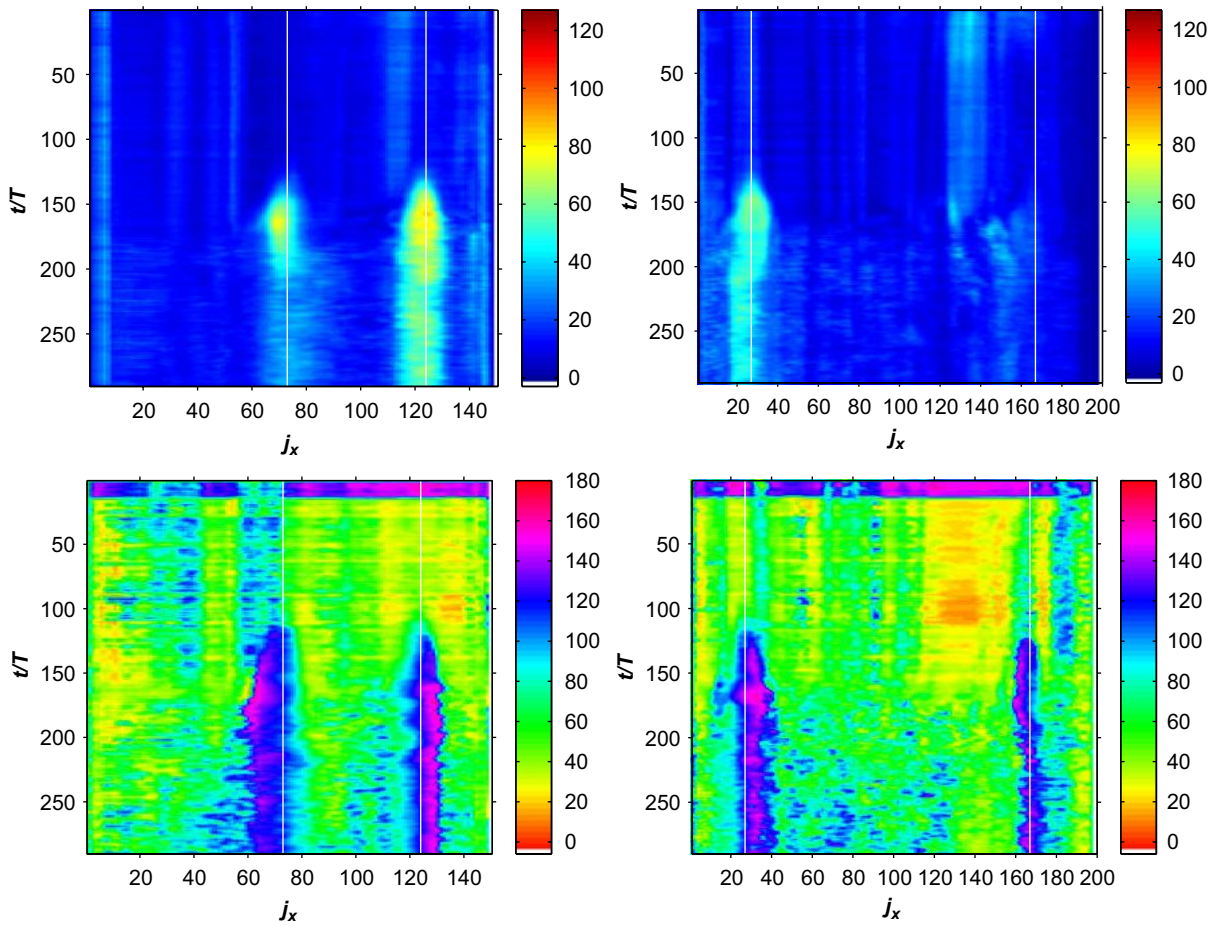

Fig. 9. As Figs. 6 and 7, but for second harmonic frequency 2ω. Amplitude (top) and phase (bottom) are given for beams crossing the long branches 1 and 3 of the attractor (left), and crossing the short branches 2 and 4 of the attractor (right).

growth commences, and the duration of the growth are independent of the location at which these are observed.

The net growth rate of $1/122\,\mathrm{s}^{-1} = 0.0082\,\mathrm{s}^{-1}$ is significantly smaller than that of waves excited in the same configuration without sloping wall, which, for the largest scale resonant mode, amounted to $0.069\,\mathrm{s}^{-1}$ (Benielli and Sommeria, 1998). The net growth rate is determined by forcing rate $s = \omega^3 Z/g$, proportional to vertical oscillation amplitude Z, minus decay rate Q. This decay rate represents interior damping due to shearing motion, Q_{inter}, plus dissipation due to boundary friction, embodied in Q_{bound}. In the rectangular domain, boundary friction dominates interior damping by a factor hundred, and the computed (observed) decay rate of the largest scale mode $Q = 1.4(2.6) \times 10^{-2}\,\mathrm{s}^{-1}$ (Benielli and Sommeria, 1998). The computed interior decay rate is $\nu k^2/2$, where k is wave number and ν molecular viscosity and the computed boundary decay rate is proportional to $(\omega\nu/2)^{1/2}/\Lambda$, where Λ is a length scale representative of the basin shape. Both increase with increasing viscosity. The small net growth rate in our container with sloping side wall is consistent with the idea that the attractor is very dissipative (Ogilvie, 2005).

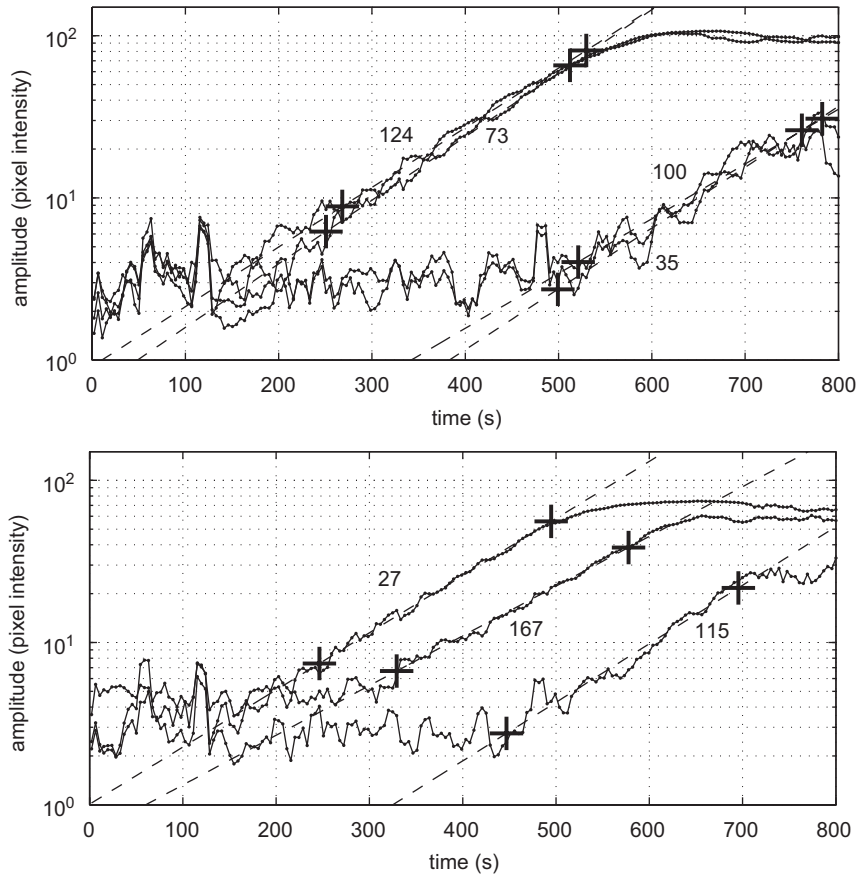

Fig. 10. Analysis of exponential growth for signals shown in Figs. 6 and 7, left and right panels, respectively. Numbers indicate four (top panel) and three (bottom) indices j_x (including the vertical lines in Figs. 6 and 7) that are representative of positions that are either on or away from an attractor branch. For all cases, the exponential factor τ_g, determined by the slope of the dashed line, is about 122 s, with pixel intensity growing as: $\exp((t - t_0)/\tau_g)$. The time intervals over which growth occurs and over which the growth rate is determined is demarcated by plus (+) symbols.

The small wave numbers associated with the wave focusing in the sloping-wall experiment suggest a substantial increase of the internal dissipation, overshadowing the reduction of boundary dissipation due to the localized nature of fluid motions accompanying the attractor. Ogilvie (2005) finds that in the presence of a wave attractor the total amount of dissipation is insensitive to the actual magnitude and form of the small-scale damping process of the waves (viscosity) and is thus set by the influx of energy.

The stronger damping also explains the smaller maximum amplitudes reached in the basin with sloping side (approximately 3.5 cm), compared to those at which the standing internal wave saturates in the rectangular tank, which can reach amplitudes in excess of 10 cm (Benielli and Sommeria, 1998). Moreover, in the rectangular tank the sloshing mode was frequently observed to become statically or parametrically unstable, leading to renewed growth over a very long time scale. In contrast, the wave attractor's final state seems fairly stable, although we anticipate that the mixing that is continuously present will lead to a long-term modification, which might bring the forcing frequency out of the period-1 attractor regime.

4. Traveling wave solution for sloshing surface forcing

4.1. Goal

In the previous section an extended, but still rather quantitative description is presented for the internal wave attractor experiment, first addressed in MBSL. It became clear that the asymptotic state reached in the experiment is that of a propagating wave. It thus seems natural to search for a theoretical asymptotic description of the stream function field that captures this propagating feature which will be presented here. Let us first list discrepancies between the present theoretical solutions (e.g. Fig. 2) and the experimental results which obstruct a direct, one-to-one, comparison:

(i) The proposed solution is only allowed to have a 'standing-wave appearance'; the stream function field in Fig. 2 is supposed to be blinking, i.e. has a binary (0° or 180°) phase.
(ii) It is difficult to associate the surface boundary condition for $f(x)$ that is needed to provide a unique solution and that is related to the surface pressure (ML) to a realistic forcing, see for instance the upper frame of Fig. 2.
(iii) It is hard to directly relate the stream function field $\psi(x, z)$ (or $\Psi(x, z, t)$ for that matter) to the observed (vertical) fluid displacement in the experiment presented in the previous section.

All three elements will be improved below. It could be objected that in the presence of wave attractors one may not expect the solution to be of a standing nature. Wunsch (1969) invoked this argument in inferring the character of internal waves in a subcritical wedge (a wedge whose slope is less than that of the characteristics). He argued that standing waves are not likely to occur, for internal waves will not reflect back from the corner; all energy is transported in just one direction, i.e. into the wedge, which therefore acts as a point-attractor. There, these waves will amplify till the point of wave breaking and will locally mix fluid. Similar reasoning can be followed for most closed basins with supercritical slopes giving rise to wave attractors: all energy is supposedly transported just towards the attractor, without being reflected back from it. ML therefore suggested to employ propagating wave solutions. This will be performed in the following.

4.2. Traveling wave solution by allowing for complex $f(x)$, $g(x)$: externally forced flow

Can we construct propagating solutions? Within the framework of free solutions, this question can be answered affirmatively by simply choosing the partial pressure as a complex quantity. Taken literally, this solution is physically not very meaningful, as it implies that waves are generated at the wave attractor, propagate away from it, against the focusing sense (anticlockwise in Fig. 1a), then pass through the bulk of the fluid and finally converge onto the attractor again, now approaching it in the focusing (clockwise) sense. But, can we use our knowledge on the existence of fundamental intervals and force waves such that they only propagate *away* from these intervals? This does indeed seem to be possible by supposing that some externally applied surface pressure field, $p_a(x)$, is given there and by subsequently decomposing this into its Fourier components. Then, in the fundamental intervals we decompose each such Fourier component further into 'rightward' and 'leftward' propagating (complex) components, using the relation

$$\cos(ax) = \tfrac{1}{2}\,\mathrm{e}^{+\mathrm{i}ax} + \tfrac{1}{2}\,\mathrm{e}^{-\mathrm{i}ax} \equiv f_{\mathrm{R}} + f_{\mathrm{L}}, \tag{3}$$

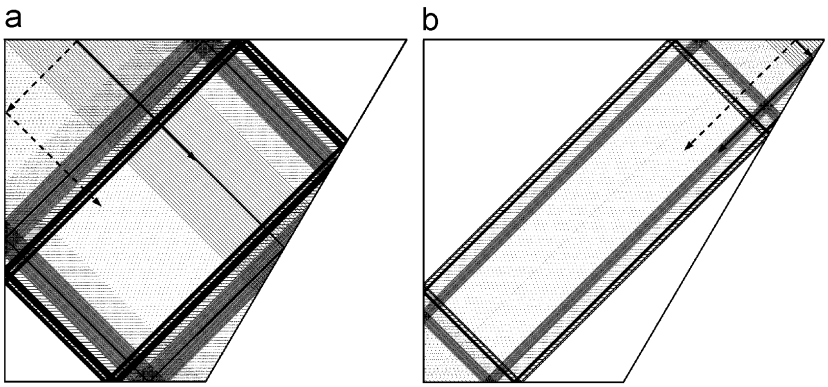

Fig. 11. Leftward (dotted) and rightward (solid) characteristics, as originating from both fundamental intervals computed for $\tau = 1.71$. The fundamental intervals at the surface are $-1 \leqslant x \leqslant -0.29$ (a, left) and $0.71 \leqslant x \leqslant 1$ (b, right), see Fig. 1b. All characteristics emanating from the fundamental interval downward and to the right (along solid arrows), appear as a black band after one focusing reflection. The lighter, dashed band of characteristics are build up of dotted lines, traveling downward and leftward (along dashed arrows) from the fundamental intervals.

for arbitrary a, and similarly for $\sin(ax)$. The designations leftward and rightward for f_{L} and f_{R} refer to the direction into which horizontal components of phase and energy propagate when multiplying by $\mathrm{e}^{-\mathrm{i}t}$ (in nondimensional form). It implies that, in contrast to the standing wave case, each web is no longer specified by a single invariant f. Instead, quantities f_{L} and f_{R} are now invariant on two *semi-infinite* webs only (obtained by following characteristics leftward or rightward, respectively, from any starting point in the fundamental interval) and should be interpreted as the (complex) f and $-g$ in the original derivation, (1). As a consequence, within the fundamental intervals, the stream function ($\psi = f - g$) and its along boundary gradient ($w = \partial\psi/\partial x$) no longer vanish. This betrays that at that part of the boundary there is a periodic motion normal to the boundary which is in phase with the applied pressure ($p_a = f + g$) and hence represents a transfer of energy across the boundary.

In order to compute the stream function in any interior point from the given data at the boundary, some bookkeeping is needed for tracing back any characteristic to the fundamental interval where it originated. Also the direction from which the fundamental interval is reached has to be traced, as this clarifies to which of the two semi-infinite webs it belongs. This can easily be seen with the help of Fig. 11, where the original leftward (rightward) characteristics are represented by dotted (solid) lines. The only exception occurs when a characteristic is exactly part of the attractor, which remains undefined; both for the stream function, as well as for $f(x)$ and $g(x)$ at the surface. After this bookkeeping, for any point (x, z), the complex-valued stream function $\psi(x, z)$ can be assigned by (1). The stream function at time t is then found from $\Psi(x, z, t) = \mathrm{Re}[\psi(x, z)\,\mathrm{e}^{-\mathrm{i}\omega t}]$. An example following this approach is given in Fig. 12 . At the surface, the same boundary condition, $p_a(x)$, is used as in Fig. 2. Here the stream function is given for six time steps; $t/T_{\mathrm{w}} = n/12$, for $n = 1, \ldots, 6$, showing half an internal wave period. Outside the (primary) fundamental intervals the stream function remains zero at the surface as well as on all other rigid boundaries (uniformly dark gray color); waves only reflect here. In the fundamental intervals, however, the stream function is no longer always vanishing. This illustrates that the vertical velocity, ψ_x, is nonvanishing in these intervals, which is in phase with the pressure perturbations so that work is done upon the fluid in these isolated intervals, similar to the action of two pistons.

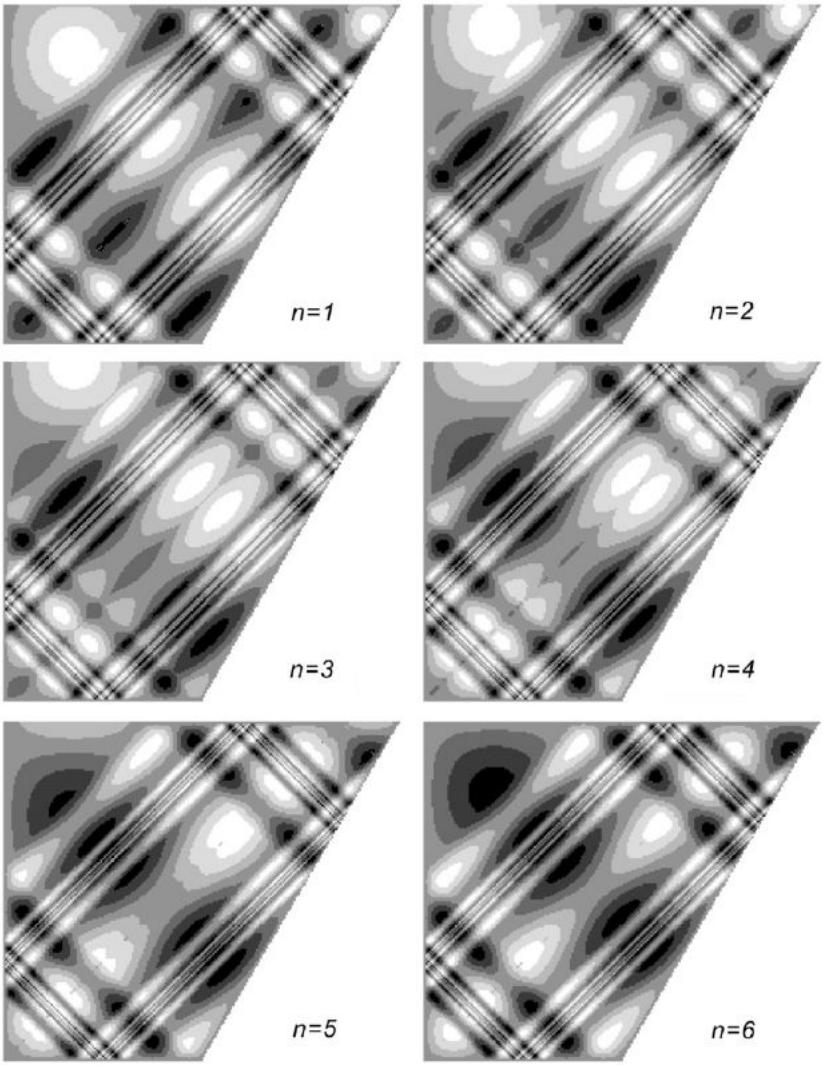

Fig. 12. Example of stream function fields at times $t/T_w = n/12$, for $n = 1, \ldots, 6$, illustrating traveling wave solution for $\tau = 1.71$. The same surface boundary pressure $p_a(x) = f(x) + g(x)$ is used as in Fig. 2, but is now understood as being composed of complex partial pressures $g(x) = f^*(x)$, where the asterisk denotes the complex conjugate. Also the same gray scale legend can be applied to these images (now for Ψ instead of ψ).

In this 'movie', we can actually see internal wave energy transferring from the fundamental intervals towards the attractor. The direction of this transfer can be verified in Fig. 12: at the surface, phase moves out of the fluid, which means that energy enters the fluid.

4.3. Boundary forcing not restricted to two fundamental intervals

In the previous subsection, the forcing of the traveling wave solution took place only in the (primary) fundamental intervals. This could be envisaged by two (flexible) pistons at the surface, which are exactly

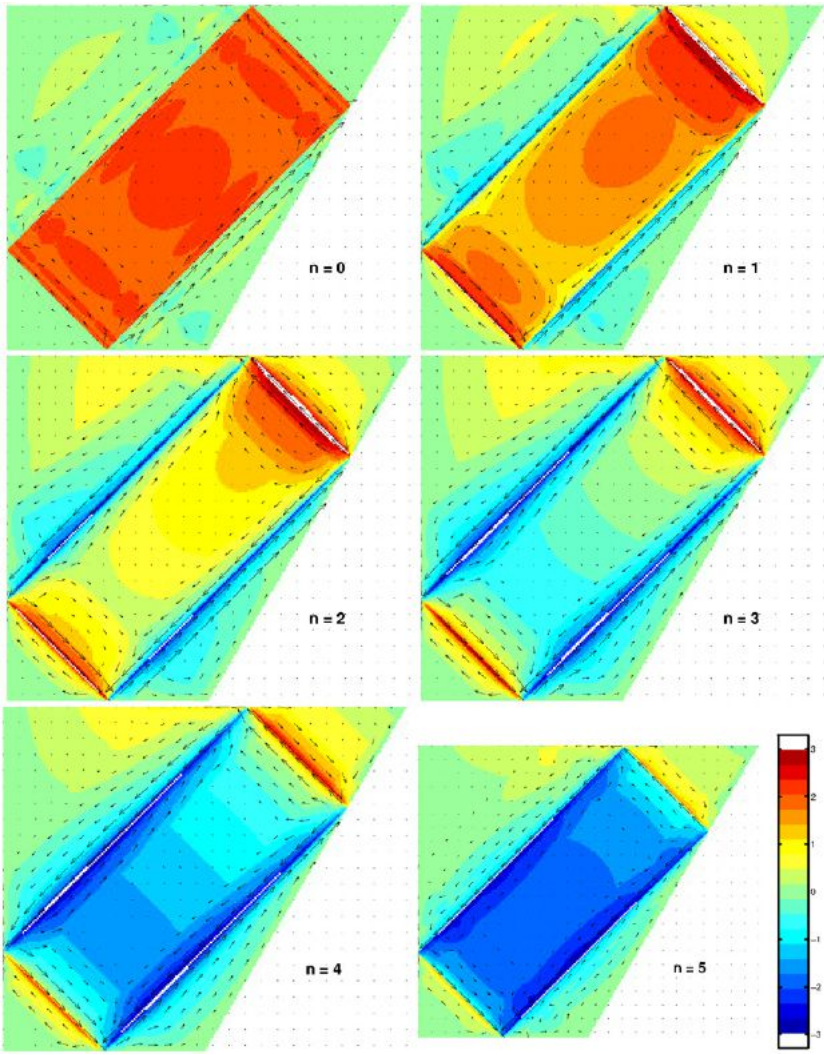

Fig. 13. Example of iteratively defined traveling wave solution $\Psi(x, z, t)$ for 'surface sloshing' boundary condition; $p_a(x) = \sin(x\pi/2)$. Times shown are for $n = 0, \ldots, 5$, with $t/T_{\mathrm{w}} = n/12$. Stream function Ψ is color-coded, as shown in the legend. Arrows represent the velocities as derived from numerically computed stream function gradients based on the stream function field.

as wide as the fundamental intervals, and which are fully isolated from the remaining surface of the fluid. In natural systems, the forcing is of course not restricted to such intervals. We therefore would like to prescribe, e.g. a surface pressure over the entire surface domain; $x \in [-1, 1]$. Think of this as representing an infinitesimal-amplitude barotropic seiche, again generated by the modulation of gravity; as in nonresonant Faraday excitation (Faraday, 1831; Drazin and Reid, 1981).

As explained in ML, when f is prescribed over the complete surface this might raise inconsistencies. For the partial pressure f that is passed along the characteristics would generally be defined multiply along

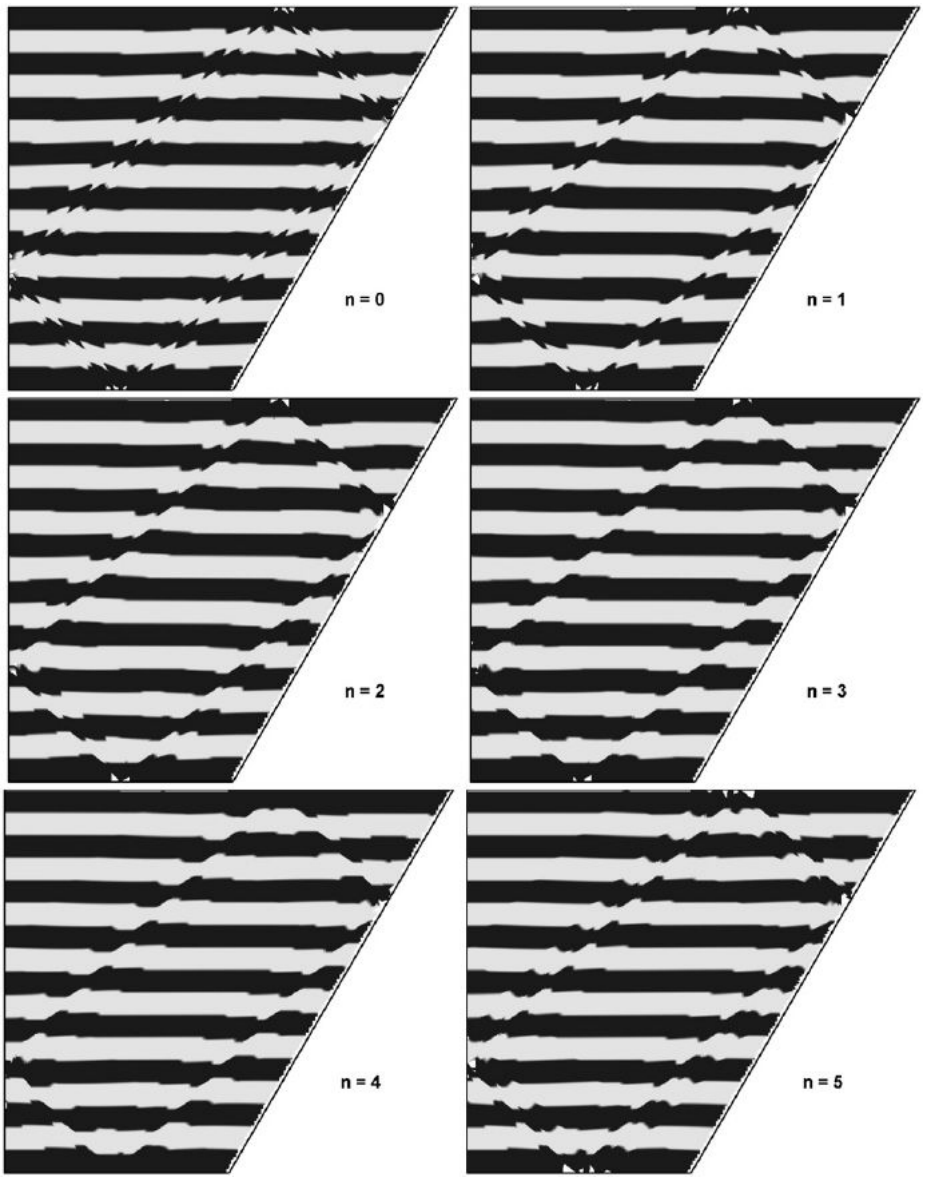

Fig. 14. Example of iteratively defined traveling wave solution $\Psi(x, z, t)$ for 'surface sloshing' boundary condition; $p_a(x) = \sin(x\pi/2)$. Here the associated displacement is shown by artificial 'dye' bands for times $n = 0, \ldots, 5$, with $t/T_w = n/12$.

any characteristic. However, since ψ is a solution to a linear problem this leaves open the possibility to superpose partial solutions ψ_n:

$$\psi = \sum_{n=1}^{N} (\psi_n + \psi_{-n}). \tag{4}$$

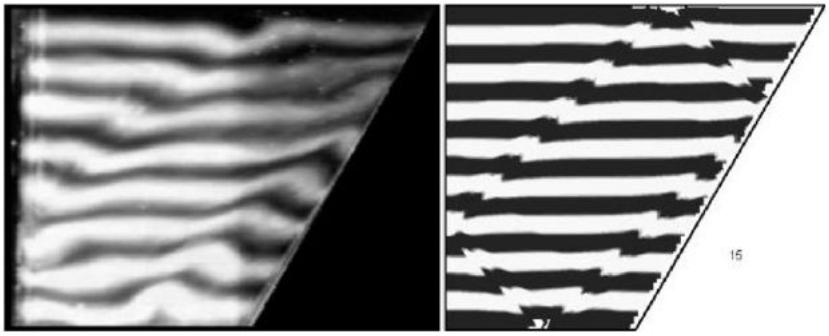

Fig. 15. Comparison of observed (left) and computed dye displacement field (right). The computed image on the right is for time: $n = 15$, but now with $t/T_w = n/24$ (the opposite phase of the virtual image between $n = 1$ and 2 in Fig. 14).

Here, each individual fundamental interval is regarded as supplying one additional component ψ_n to the total solution. The two primary fundamental intervals supply ψ_1 and ψ_{-1}, their next-neighboring fundamental intervals, found by following the boundaries of the primary intervals right and left wards, supply ψ_2 and ψ_{-2}, and so on. If we now want to impose the surface boundary condition over the complete surface, one more physical assumption needs to be made: we assume that at each point of the surface, work is done only by the prescribed pressure, not by the pressure variations induced at that location by forcing elsewhere. Following the characteristics, the (complex) partial pressure that is thus set on each characteristic will simply be passed on upon successive boundary (surface) reflections. In other words: for each contribution ψ_n, the external boundary condition is applied once, and reflects from there on. Physically, this means that at the surface the boundary condition is imposed, while the surface's reflective nature is unaffected! Although this may apply only for small perturbations at the boundary, in general this is not an uncommon situation. This also happens when forcing a string that is fixed at one end resonantly, by periodically shaking the other end (with infinitesimal amplitude). At the latter, forced end of the string, energy is both entering the system as well as reflecting there, enabling the build up of a standing wave.

In fact, (4) can also be viewed as directly supplying the stream function at any particular point, (x, z), in the interior of the domain. In this interpretation, the ψ_n supplies the partial pressure, set in the nth fundamental interval. This is there obtained from the applied pressure, regarded to be specified over the whole surface $p_a = f + g$. Starting from any point, (x, z), we can define the components of (4) as follows: ψ_1 is defined by the forcing on the first two surface reflections of the two upward characteristics that cross at (x, z); ψ_{-1} by the downward pair of characteristics crossing at (x, z) that reach the surface upon bottom and side-wall reflections. $\psi_{\pm n}$ for $n = 2, \ldots, N$ are defined similarly, by following these characteristics further, until their next n surface reflections. The method converges (and the solution is bounded). When n is large, $\psi_{\pm n}$ does not contribute to ψ anymore, for, when the attractor is nearly reached, values of the prescribed surface pressure $f + g$ (assumed to be smooth) are nearly equal. So their difference, as defined by (1), vanishes. Only at the locations of the characteristics that describe the single periodic orbit associated with the attractor the solution and the boundary condition are undefined.

With the alternative algorithm, described above, also the standing wave solution of Fig. 2 can be obtained (for which $g(x) = f(x)$) if $f(x)$ is real and nonvanishing only in the primary intervals. Previously, by employing the invariance of $f(x)$ per web we constructed the partial pressure $f(x)$ over the whole surface (excluding the reflection point of the attractor) by iteration from the two fundamental intervals. The stream function was then read off in any point as the difference of the two invariants that were defined by their

values at the first two upward surface intersections. Here, instead, from each field point one iterates backwards until one arrives in a fundamental interval in order to determine the partial pressure.

This approach more naturally allows the partial pressure to be prescribed differently in different fundamental intervals, allowing for the description of propagating wave solutions, see Swart et al. (2007). In this process, not only each of the four directions from which waves can reach the point of interest should be considered, but also one should determine at each surface reflection whether the leftward or rightward part f_L or f_R should be chosen. Doing so, we get a complete traveling wave solution for Ψ for an arbitrarily defined surface forcing. An example of this is given in Fig. 13 in which the applied surface pressure is chosen as: $p_a = \sin(x\pi/2)$; this is the lowest mode of a (surface) seiche (for a rectangular basin). We will refer to this type of forcing as 'surface sloshing'. This could be thought of as the first Fourier component of a surface sloshing mode for this trapezoidal basin. The only additional (physical) restriction at the surface, $z = 0$, is that $\partial p_a/\partial x(\pm 1) = 0$, because the corners are stagnation points where $u(\pm 1) = 0$. This condition also prevents the appearance of internal shear layers (see Fig. 20a of ML for an example of this effect).

4.4. Approximate fields for velocity and displacement

In order to make a comparison with the displacement of the horizontal dye bands in the laboratory experiment (Section 3) we will now compute the displacement field associated with the traveling wave solution of Fig. 13. This is done in a pragmatic way. From the stream function field Ψ, the fields for the velocity components u and w are derived, see vector fields in Fig. 13. In this example, the gradient of Ψ is computed numerically. After that, the displacement is approximated by a simple linear Taylor approximation: $x = x_0 + u(x_0)\Delta t$ and $z = z_0 + w(z_0)\Delta t$, for an arbitrary time increment Δt, and with original position (x_0, z_0). Fig. 14 gives an example, where the position of eight originally horizontal dye bands in the fluid are visualized (suppressing locations outside the domain in this linear approximation). This figure reveals that the waves get focused near the attractor.

Fig. 15 shows there is good overall agreement between the laboratory experiment and the 'simulation'. The location of the attractor is clearly visualized and its width is, geometrically speaking, to first order defined by the first surface reflection of the fundamental interval. This is visualized by the largest black band in Fig. 11. Also some fine scale structure is visible in both cases, with a scale defined by the next surface reflection of the fundamental interval. But in the experiment finer scales are suppressed, probably by viscosity.

Some other choices for the boundary condition were explored, especially the case $p_a = \cos(\pi x)$, where, contrary to the previous example, the outer regions are in-phase at the surface. However, the first example has more resemblance with the laboratory experiment.

5. Summary and discussion

5.1. Brief summary of results

In Section 3 the laboratory experiment, described in MBSL, was reanalyzed. More details in space and time about the amplitude and phase of the internal oscillations were revealed and quantified. Several limitations of the experimental setup were explored and mostly understood. The appearance of the internal

wave attractor and its temporal and spatial development were clearly visualized this way. The overall inverse exponential growth rate was found to be 122 s, starting later outside the attractor neighborhood.

In Section 4 the theoretical description of a monochromatic internal wave field of a stratified, confined, essentially two-dimensional free-surface fluid (ML,MBSL) was extended to include traveling wave solutions. By an iterative approach, also more generic (and more realistic) boundary conditions can be applied. Finally, visualization of displacement fields, as obtained by Taylor approximations of velocities (obtained from numerical estimates of the gradients of the analytically predicted stream function field), made a better comparison possible to the actual experimental displacements. The closer resemblance between the two was based on assuming that the theoretical field was forced by a small amplitude surface seiche.

5.2. Discussion

The reanalysis of the earlier observations reveals a number of new interesting facets regarding the formation of an internal wave attractor. Fig. 10 showed that the wave field exhibits phenomena known from related studies on parametrically excited waves (Miles and Henderson, 1990; Benielli and Sommeria, 1998; Hill, 2002): (1) slow growth above the noise level, (2) a rapid exponential growth phase, (3) a slight overshoot, and (4) saturation into a quasi-steady asymptotic state. These features are usually properties of the time-dependent amplitude field of a spatially fixed, standing wave structure. As a consequence, in such circumstances each field point exhibits these phenomena simultaneously (no spatial delay). The spatial structure of the field acts as a local weighting factor and determines the local saturation level. The amplitude equation is often a nonlinear Landau type of equation (Benielli and Sommeria, 1998), whose steady state is obtained when nonlinearity together with dissipative and dispersive terms balance the parametric excitation. It can be used to infer the strength of interior and boundary damping processes.

However, the novel property encountered in the wave attractor is that there is no spatial eigenmode structure and that, indeed, in the final stage the wave is not standing at all. Compared with the growing standing mode this distinctive property is visible in that different spatial positions exhibit (1) equal growth rates, (2) different delays, (3) different durations of growth periods. This is in consonance with expectations based on linear partial differential equations proposed to describe internal wave beams (Dauxois and Young, 1999; Tabaei and Akylas, 2003; Voisin, 2003). These descriptions typically incorporate viscous and diffusive processes, balancing dispersive effects, that may explain the observed delayed growth and reduced growth duration outside the direct vicinity of the wave attractor.[3] Such a PDE model is by itself not able to explain the appearance of a stationary state. This also requires a persistent internal wave source, e.g. an oscillating cylinder, as in experiments by Makarov et al. (1990). In the wave attractor case, geometric focusing acts as such a ‘source’ term. Its amplification balances the viscous spreading that occurs along most of the attractor of the internal wave field. This was cleverly build into models by Rieutord et al. (2002) and Ogilvie (2005). In the present experiment, however, it seems that viscosity is not the relevant damping process, but that damping is instead dominated by internal wave scattering upon reflection from the free surface. This suggestion is motivated by observing that the width and amplitude

[3] Note that nonlinearity has not been discarded from these models, but the slow-time amplitude equation turns out to be linear, even though the nonlinear generation of the second harmonic and mean fields are necessary intermediaries. It is significant that the internal wave observations presented here also exhibit second harmonic (see Fig. 9) and mean (not shown) fields that are present around the location where the attractor of the fundamental harmonic is situated.

of the wave beam are nearly constant around the attractor, except suddenly on the final, fourth branch, where the amplitude has dropped significantly and where wave growth appears later in time. Compare e.g. the delayed exponential growth on this branch, evidenced in Fig. 10b by the curve labeled 167, to that on the other three branches (labels 124, 27 and 73, respectively). Also, the second harmonic is absent on this fourth branch, see upper right panel of Fig. 9.

A referee suggested that the atypical, spatially varying growth may have been excited by many eigenmodes. However, we want to stress that eigenmodes (and eigenfrequencies) do not really exist in these spatially hyperbolic systems (ML). In other words, the eigenspectrum can (depending on taste) be said to be either empty or continuous. Fact is that whatever frequency in the internal wave frequency range is impressed on the system, the fluid responds at *that* frequency in the manner observed; that is, it will grow initially as a standing mode, and upon saturation slowly transform into a propagating wave. Its spatial structure cannot be related to that of an eigenmode (as this does not exist) but always shows the localization associated with the approach of the wave attractor. We unfortunately lack a model that captures this transition, and are thus unable to clearly understand the transition time scale (of about 170 T). Further work is needed here.

Not all problems with the experimental setup could be overcome. Light conditions and instabilities of camera position or digitizing device appeared to be not optimal. The tracer that was used, namely fluorescent dye, inhibits a direct translation from color intensity to actual (vertical) displacement of fluid particles. However, the analysis as presented in Section 3 showed that harmonic analysis provided many valuable details of the experiment, even though neither the passage of nodal lines, nor the transition from standing to traveling wave was as clearly visible as in the snapshots in MBSL, see also bottom panels of Fig. 3. It seems that nonlinear processes (a nonsinusoidal response), or nonlinear properties of the tracer that was used, may have enhanced these features in the original images over those displayed by the harmonic field. These processes are probably also the reason why the amplitude and phase fields of the second harmonic were most significant in the vicinity of the wave attractor whose location was set by the primary harmonic.

Nevertheless, the above results are an important step forward for a better understanding of the internal wave field in a confined, stratified and free-surface fluid and may direct the set-up of future experiments. Moreover, the theoretical extensions provide better possibilities for comparison with observations, both in the laboratory, as well as in (pit) lakes and in the ocean (Fricker and Nepf, 2000; Thorpe, 2003; Boehrer and Stevens, 2005).

Acknowledgments

We are grateful to Joel Sommeria and Dominique Benielli for permitting us to reuse the original data from MBSL. We thank Frans Eijgenraam for digitizing the video, and Uwe Harlander and Jeroen Hazewinkel for comments on an earlier version of the manuscript.

Appendix A. Image and time series analysis

In this appendix we give some details on the image and time series analysis. Further details can be found in Lam (2007).

A.1. Time series of gray scale intensity

Color information of the images contained in the three RGB-fields (red-green-blue) is translated to standard gray scale images, with intensity on a scale from 0 to 255. With the resulting gray scale intensities, time series can be retrieved for any position in the image. Some examples of two nearby pixels are shown in Fig. A1.

The analysis shows that pixel intensity grows in time. But, despite closeness of pixels, this growth starts at different moments and lasts for different durations. However, the growth rate appears to be quite uniform. Horizontal and vertical positions are labeled in pixel units, i_x and i_z, respectively. Time is scaled with $T = 4.36$ s, which is an integer number (109) of sampling periods (0.04 s) closest to the internal wave period of $T_w = 4.37$ s. Here time series are depicted for two positions in the image-pixel-frame: $(i_x, i_z) = (060, 115)$ and (060, 120). Fig. A1c,d shows that the second (lower) pixel resides close to the white band (near intensity 240; the lightest color, before translating to gray scale, is originally yellow) and the first pixel lies close to the dye-less black band (near intensity 80). The two disruptions in light intensity in intervals $15 < t/T < 30$ and $65 < t/T < 75$ are due to external perturbations and are ignored here. Gray scale amplitude grows in time, but, despite the closeness of the two pixels, with different starting times and possibly different growth rates. Quantification of the growth rate is given in Section 3.5. Eventually, light intensity oversaturates or undersaturates. This inhibits a correct estimate of the amplitude of the pixel intensity variation, see the enlargement in Fig. A1e, which shows this peak truncation. Another problem is that when displacements are large, dye from a second layer above or below may cause a renewed increase in pixel intensity. Superficially this suggests that the wave field develops a second harmonic, but this really bears testimony to the large wave amplitude, see Fig. A1f.

In spite of this, Fig. A1 shows that one can still obtain the location of the attractor as well as the exponential growth of the amplitude of the oscillation. In our analysis we use pixel intensity to represent the vertical component of the oscillation of fluid parcels.

A.2. Harmonic analysis

In order to obtain the characteristics of the periodic motion of the fluid, we perform a harmonic analysis to the time series of the gray scale pixel intensity. This provides the amplitude and phase of a (sinusoidal) motion having a specific well-defined period. For the laboratory experiment we will explore harmonic analysis output at every pixel position, so that we obtain the spatial distribution of amplitude and phase.

By performing harmonic analysis over 290 subsequent intervals ('sequences') of approximately one internal wave period ($T_w = 4.37$ s) each, we can follow the evolution of these fields, see Fig. A2 . In this harmonic amplitude field, we see that the rectangular shape of the internal wave attractor, consisting of four branches, becomes visible well before $t/T = 80$ (about 5 min). The attractor grows and gets more distinguished from $t/T = 100$–130 (7.3–9.4 min). After that, overall amplitudes equilibrate, and the regions of higher amplitudes smear out somewhat over the image and also influence the region outside the attractor region.

A.3. Phase ambiguity

In the harmonic analysis, phase is computed in three steps. The first step computes the phase per pixel, based on the pixel intensity. Fig. A3a shows an example of this harmonic phase, taken at $t/T = 160$.

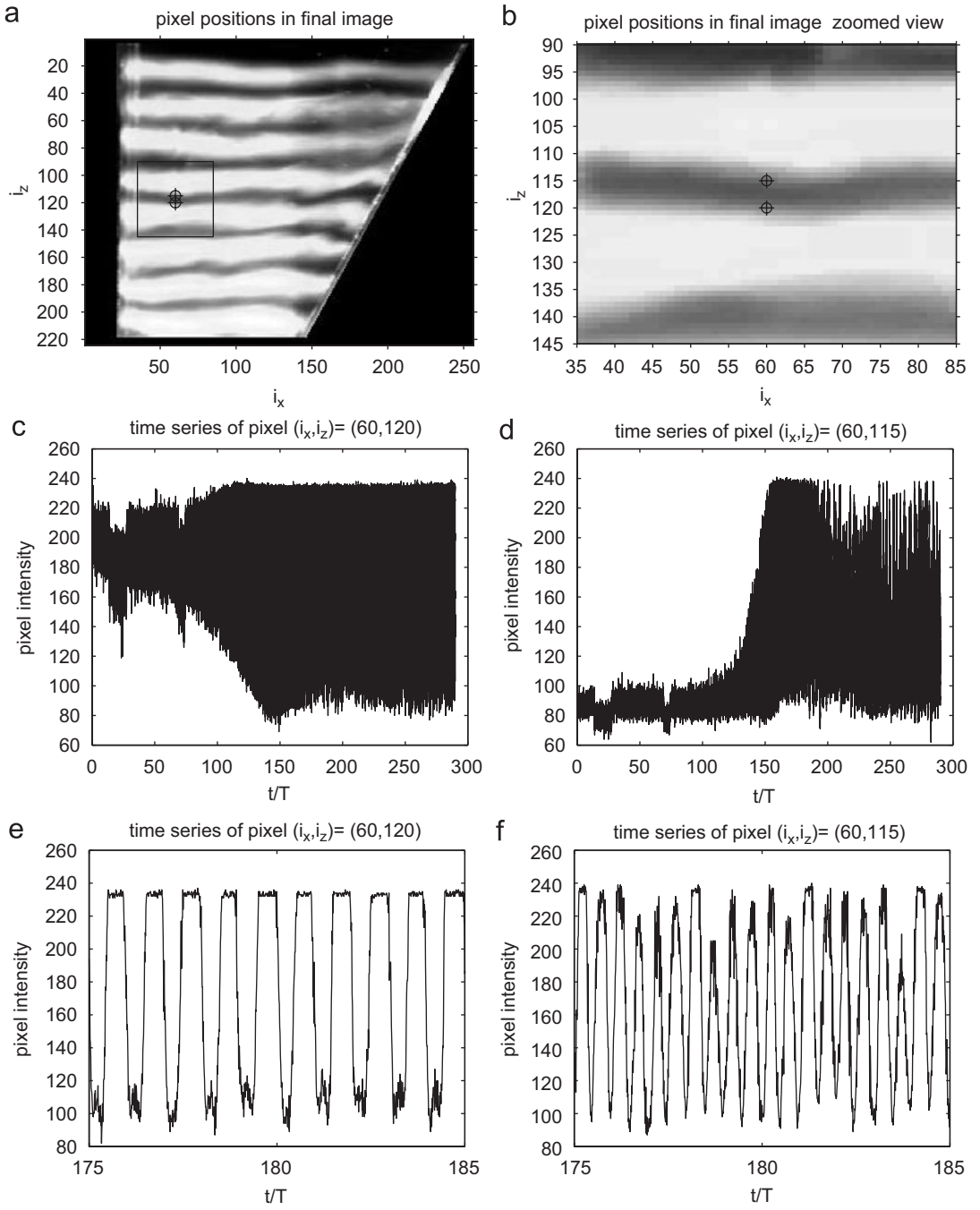

Fig. A1. Two positions (a, zoomed in b), with their pixel intensity time series (c,d) and zoomed view of these time series (e,f).

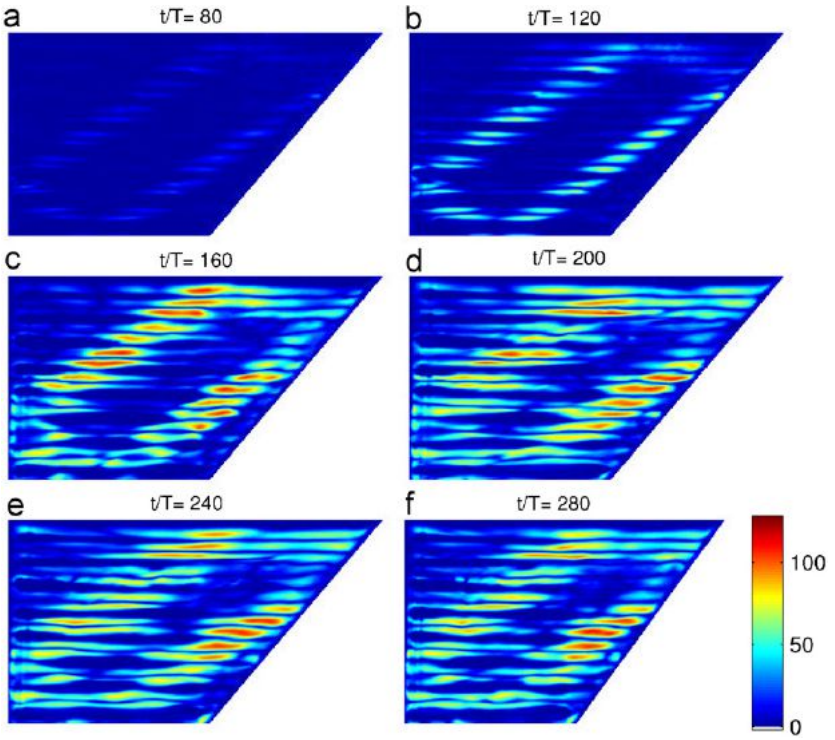

Fig. A2. Evolution of harmonic amplitude of pixel intensity (color coded, see legend). Scaled time t/T at the middle of time series is given above each image. These times correspond to the following dimensional times: $t = 347$, 521, 695, 870, 1044 and 1219 s.

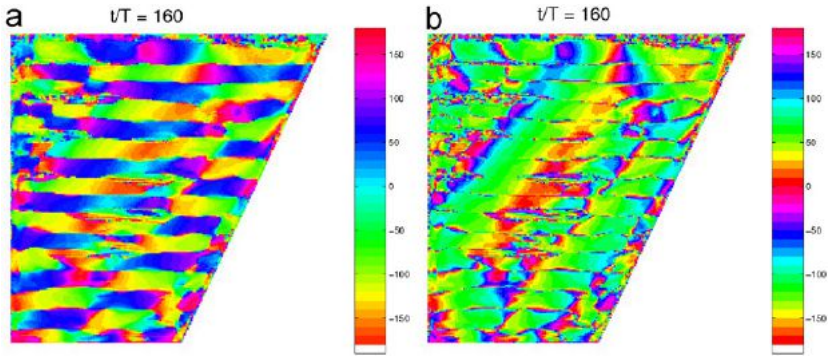

Fig. A3. (a) Evolution of harmonic phase of pixel intensity. Color coded phase in degrees, see legend. Same time of images as in Fig. 4 and Fig. A2c: $t/T = 160$. (b) Same as in (a), but now the (double) color map is modulo 180° (see legend). This color map masks the elevation/depression ambiguity for the pixel intensity.

Phase is defined relative to $t/T = 0$. Changes in pixel intensity around every dye interface are out of phase with those around the next interface when elevations along the attractor are in phase, because intensity increases at one interface (e.g. dark above light) and decreases at the next interface (thus, light above dark). Note that the pixel intensity is also out-of-phase at the opposing branch of the attractor: an in-phase

elevation along branch 3 of the attractor is accompanied with an in-phase depression along branch 1 (and *vice versa*).

In the second step, the former out-of-phase behavior between subsequent interfaces is eliminated by applying a color map mod π instead of 2π, see Fig. A3b. Now the regular shape of the attractor can be better appreciated, but the out-of-phase character of opposite attractor branches is lost.

In the third step, we add π to the phase around all even interfaces, leaving the odd interfaces intact. Fig. 4b shows the result of correcting phases around even interfaces, after having defined the interface position adaptively for each phase image (like e.g. Fig. A3a). In order to get a coherent overview, phase is smoothed by taking the median value of 25 neighboring pixels for each pixel leading to Fig. 4b. Especially, the out-of-phase character of the two pairs of opposite attractor branches can now be appreciated.

References

Baines, P.G., 1997. A fractal world of cloistered waves. Nature 388 (6642), 518–519.

Bender, C.M., Orszag, S.A., 1978. Applied Mathematical Methods for Scientists and Engineers. McGraw-Hill, New York.

Benielli, D., Sommeria, J., 1998. Excitation and breaking of internal gravity waves by parametric instability. J. Fluid Mech. 374, 117–144.

Boehrer, B., Stevens, C., 2005. Ray waves in a pit lake. Geophys. Res. Lett. 32 (24), L24608.

Dauxois, T., Young, W.R., 1999. Near-critical reflection of internal waves. J. Fluid Mech. 390, 271–295.

Drazin, P.G., Reid, W.H., 1981. Hydrodynamic Stability. Cambridge University Press, Cambridge.

Faraday, M., 1831. On a peculiar class of acoustical figures: and on certain forms assumed by groups of particles upon vibrating elastic surfaces. Philos. Trans. R. Soc. London 121, 299–340.

Fricker, P.D., Nepf, H.M., 2000. Bathymetry, stratification, and internal seiche structure. J. Geophys. Res. 105 (C6), 14237–14251.

Gerkema, T., 2001. Internal and interfacial tides: beam scattering and local generation of solitary waves. J. Mar. Res. 59, 227–255.

Gostiaux, L., Dauxois, T., Didelle, H., Sommeria, J., Viboux, S., 2006. Quantitative laboratory observations of internal wave reflection on ascending slopes. Phys. Fluids 18 (056602), doi: 10.10631/1.2197528.

Groen, P., 1948. Two fundamental theorems on gravity waves in the ocean. Physica 14, 294–300.

Harlander, U., Maas, L.R.M., 2006. Characteristics and energy rays of equatorially trapped, zonally symmetric internal waves. Meteor. Z. 15, 439–450.

Hill, D.F., 2002. The Faraday resonance of interfacial waves in weakly viscous fluids. Phys. Fluids 14 (1), 158–169.

Kopecz, S., 2006. Fractal internal wave patterns in a tilted square. Unpublished Report, Kassel University ⟨http://www.nioz.nl/kopecz⟩.

Lam, F.P.A., 2007. Ocean and laboratory observations on waves over topography. Ph.D. Thesis, Utrecht University.

Lighthill, S.J., 1978. Waves in Fluids. Cambridge University Press, Cambridge.

Maas, L.R.M., 2005. Wave attractors: linear yet nonlinear. Int. J. Bifurcation Chaos 15 (9), 2757–2782.

Maas, L.R.M., Lam, F.-P.A., 1995. Geometric focusing of internal waves. J. Fluid Mech. 300, 1–41.

Maas, L.R.M., Benielli, D., Sommeria, J., Lam, F.-P.A., 1997. Observation of an internal wave attractor in a confined, stably stratified fluid. Nature 388 (6642), 557–561.

Makarov, S.A., Neklyudov, V.I., Chashechkin, Y.D., 1990. Spatial structure of two-dimensional monochromatic internal wave-beams in an exponentially stratified fluid. Izvestiya 26, 548–553.

Manders, A.M.M., Duistermaat, J.J., Maas, L.R.M., 2003. Wave attractors in a smooth convex enclosed geometry. Physica D 186 (3–4), 109–132.

Miles, J., Henderson, D., 1990. Parametrically forced surface waves. Ann. Rev. Fluid Mech. 22, 143–165.

Ogilvie, G.I., 2005. Wave attractors and the asymptotic dissipation rate of tidal disturbances. J. Fluid Mech. 543, 19–44.

Peacock, T., Tabaei, A., 2005. Visualization of nonlinear effects in reflecting internal wave beams. Phys. Fluids 17 (6), article 061702 (4 pages).

Rieutord, M., Noui, K., 1999. On the analogy between gravity modes and inertial modes in spherical geometry. Eur. Phys. J. B 9, 731–738.

Rieutord, M., Valdettaro, L., Georgeot, B., 2002. Analysis of singular inertial modes in a spherical shell: the slender toroidal shell model. J. Fluid Mech. 463, 345–360.

Swart, A.N., Sleijpen, G.L.G., Maas, L.R.M., Brandts, J., 2007. Numerical solution of the two dimensional Poincaré equation. J. Comput. Appl. Math. 200, 317–341.

Tabaei, A., Akylas, T.R., 2003. Nonlinear internal gravity wave beams. J. Fluid Mech. 482, 141–161.

Thorpe, S.A., 2003. A note on standing internal inertial gravity waves of finite amplitude. Geophys. Astrophys. Fluid Dyn. 97 (1), 59–74.

Turner, J.S., 1973. Buoyancy Effects in Fluids. Cambridge University Press, Cambridge.

Voisin, B., 2003. Limit states of internal wave beams. J. Fluid Mech. 496, 243–293.

Wunsch, C., 1969. Progressive internal waves on slopes. J. Fluid Mech. 35, 131–141.